OPEN ACCESS



Properties of the Lowest-metallicity Galaxies over the Redshift Range z = 0.2 to z = 1

Isaac H. Laseter ¹, Amy J. Barger ^{1,2,3}, Lennox L. Cowie ², and Anthony J. Taylor ¹ Department of Astronomy, University of Wisconsin-Madison, 475 North Charter Street, Madison, WI 53706, USA; laseter@wisc.edu

² Institute for Astronomy, University of Hawaii, 2680 Woodlawn Drive, Honolulu, HI 96822, USA

³ Department of Physics and Astronomy, University of Hawaii, 2505 Correa Road, Honolulu, HI 96822, USA *Received 2022 February 2; revised 2022 June 14; accepted 2022 July 14; published 2022 August 23*

Abstract

Low-metallicity galaxies may provide key insights into the evolutionary history of galaxies. Galaxies with strong emission lines and high equivalent widths (rest-frame EW(H β) \gtrsim 30 Å) are ideal candidates for the lowest-metallicity galaxies to $z \sim 1$. Using a Keck/DEIMOS spectral database of about 18,000 galaxies between z=0.2 and z=1, we search for such extreme emission-line galaxies with the goal of determining their metallicities. Using the robust direct T_e method, we identify eight new extremely metal-poor galaxies (XMPGs) with $12 + \log O/H \leqslant 7.65$, including one at 6.949 ± 0.091 , making it the lowest-metallicity galaxy reported to date at these redshifts. We also improve upon the metallicities for two other XMPGs from previous work. We investigate the evolution of $H\beta$ using both instantaneous and continuous starburst models, finding that XMPGs are best characterized by continuous starburst models. Finally, we study the dependence on age of the buildup of metals and the emission-line strength.

Unified Astronomy Thesaurus concepts: Observational cosmology (1146); Galaxy abundances (574); Starburst galaxies (1570); Galaxy evolution (594)

1. Introduction

Low-redshift ($z\lesssim 1$), low-metallicity galaxies could be the best analogs of small, star-forming galaxies (SFGs) at high redshifts ($z\gtrsim 6$). Such low-redshift galaxies may give insights into the properties of early SFGs, which may be responsible for reionizing the universe. Izotov et al. (2021) found that the properties of low-metallicity, compact SFGs with high equivalent widths (EWs) of the H β emission line are similar to the properties of high-redshift SFGs.

The lowest-metallicity galaxies are often called extremely metal-poor galaxies (XMPGs). These are defined as galaxies with metallicities $12 + \log \mathrm{O/H} \leqslant 7.65$, which is 1/10 of the solar metallicity (8.65; Asplund et al. 2006). A few dozen local XMPGs have been discovered, with the lowest-metallicity galaxies being IZw18 at 7.2 (Sargent & Searle 1970), SBS 0335-052W at 7.1 (Izotov et al. 2005), and J0811 + 4730 at 7.0 (Izotov et al. 2018). Recent work by Senchyna et al. (2019) report metallicities down to 7.25, and Nakajima et al. (2022) down to 6.86.

For $z\lesssim 1$, XMPGs can be found by targeting extreme emission-line galaxies (EELGs) with high rest-frame EWs of H β (hereafter, EW $_0$ (H β) > 30 Å). To achieve such high EWs, galaxies must have intensive star formation. EELGs are relatively common at z=0.2–1 (e.g., Hoyos et al. 2005; Kakazu et al. 2007; Hu et al. 2009; Salzer et al. 2009, 2020; Ly et al. 2014; Amorín et al. 2014, 2015) and contain a significant fraction ($\sim 5\%$) of the universal star formation at these redshifts (Kakazu et al. 2007; Hu et al. 2009). The lowest-metallicity galaxies from the EELG samples between z=0.2–1 are KHC912-29 at 12 + log(O/H) = 6.97 \pm 0.17 and KHC912-269 at 7.25 \pm 0.03 (Hu et al. 2009). Low-redshift EELGs have been found with narrowband, grism, and color selections. An

Original content from this work may be used under the terms of the Creative Commons Attribution 4.0 licence. Any further distribution of this work must maintain attribution to the author(s) and the title of the work, journal citation and DOI.

example of the latter are the Green Pea galaxies found in shallow Sloan Digital Sky Survey (SDSS) broadband imaging data (Cardamone et al. 2009). A recent analysis of color selections using deep Subaru/Hyper Suprime-Cam broadband imaging data can be found in Rosenwasser et al. (2022).

Here we use a different approach to the problem, which is more analogous to choosing objects out of the SDSS spectroscopic sample but at considerably fainter magnitudes. We work with an archival sample of galaxies with spectra from Keck/DEIMOS, selecting those with high EW₀(H β) and redshifts z=0.2-1. Our main goal is to obtain a significant sample of XMPGs with strong [O III] λ 4363 detection where we can use the "direct T_e method" (e.g., Seaton 1975; Pagel et al. 1992; Pilyugin & Thuan 2005; Izotov et al. 2006; Yin et al. 2007; Kakazu et al. 2007; Liang et al. 2007; Hu et al. 2009).

We organize the paper as follows: In Section 2, we describe the spectroscopic observations. In Section 3, we present our EW and flux measurements, our electron temperature determinations, our metal abundance measurements, and our error analysis. In Section 4, we give our final XMPG catalog and discuss our results. We give a summary in Section 5. We use a standard $H_0 = 70 \text{ km s}^{-1}\text{Mpc}^{-1}$, $\Omega_m = 0.3$, $\Omega_{\Lambda} = 0.7$ cosmology throughout the paper.

2. Spectroscopic Observations

During the last ~20 yr, our team obtained spectroscopy of galaxies in a number of well-studied fields (e.g., GOODS, COSMOS, SSA22, the North Ecliptic Pole, etc.) for a variety of projects (e.g., Cowie et al. 2004; Cowie & Songaila, A 2016; Kakazu et al. 2007; Cowie & Barger 2008; Barger et al. 2008, 2012; Wold et al. 2014, 2017; Rosenwasser et al. 2022) using the Deep Extragalactic Imaging Multi-Object Spectrograph (DEIMOS; Faber et al. 2003) on the Keck II 10 m telescope. The observational setup of the ZD600 line per millimeter grating blazed at 7500 Å and a 1" slit gives a spectral resolution of ~4.5 Å and a wavelength coverage of 5300 Å. However, for an individual spectrum, the specific

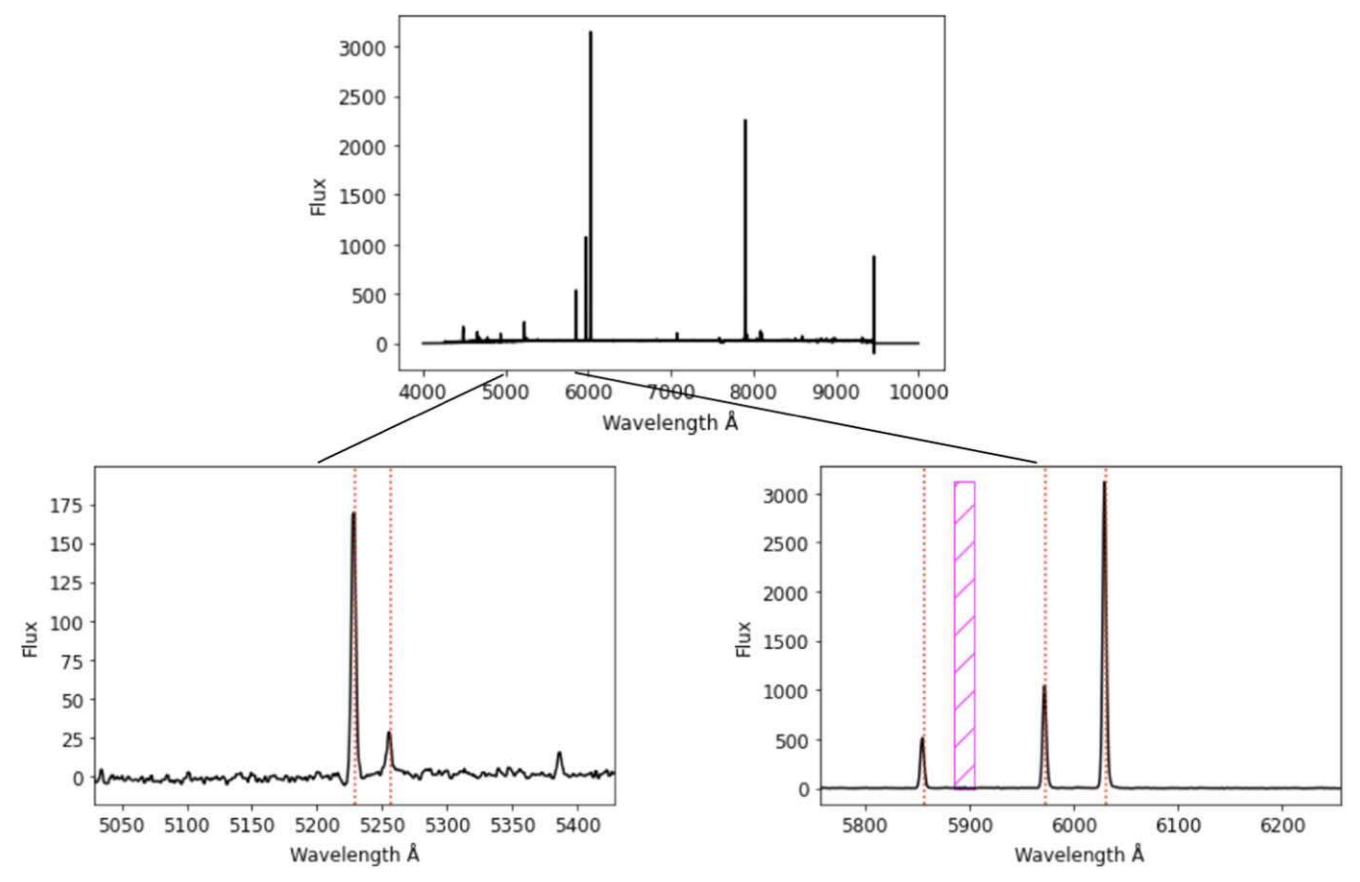


Figure 1. Example DEIMOS spectrum for a galaxy in our sample (R.A.(J2000) = 3 32 41.8, decl.(J2000) = -28 11 25.10, and z = 0.2044). (Top) Complete spectrum. (Bottom left) Portion of spectrum covering H γ and [O III] λ 4363. (Bottom right) Portion of spectrum covering H β , [O III] λ 4959, and [O III] λ 5007. The red dotted lines correspond to the wavelengths of the lines at the measured redshift. The pink hatched region marks the location of a sky line. The flux units are arbitrary, as the DEIMOS spectra are not photometrically calibrated.

wavelength range is dependent on the slit position with respect to the center of the mask along the dispersion direction. The spectra have an average central wavelength of 7200 Å.

The observations were not generally taken at a parallactic angle, since the position angle was determined by the mask orientation. Each $\sim\!60$ minute exposure was broken into three 20 minute subsets, with the objects dithered along the slit by 1."5 in each direction. The spectra were reduced and extracted using the procedures described in Cowie et al. (1996). In Figure 1, we show an example spectrum to illustrate the quality of the DEIMOS spectra obtained.

The overall spectral sample consists of ${\sim}52,\!000$ galaxies with measured redshifts, of which ${\sim}18,\!000$ lie between z=0 and z=1. We performed a preliminary $\mathrm{EW}_0(\mathrm{H}\beta)$ measurement for all ${\sim}18,\!000$ galaxies to obtain a high- $\mathrm{EW}_0(\mathrm{H}\beta)$ sample. We found 435 galaxies with $\mathrm{EW}_0(\mathrm{H}~\beta) > 30~\mathrm{\mathring{A}}$. We next removed any galaxies with incomplete spectral coverage of [O III] $\lambda\lambda5007,~4959$ or [O II] $\lambda3727,$ or where spectral lines are affected by Telluric contamination (e.g., 5579, 5895, 6302, 7246 $\mathrm{\mathring{A}},~A\text{-band}~(7600~\mathrm{\mathring{A}}\text{-}7630~\mathrm{\mathring{A}}),$ and $B\text{-band}~(6860~\mathrm{\mathring{A}}\text{-}6890~\mathrm{\mathring{A}})),$ which resulted in a final sample of 380 galaxies. We hereafter refer to this as "our sample."

In Figure 2, we present the redshift distribution for our sample. There are two peaks that correspond to narrowband filter selection at z = 0.63 and z = 0.83. A substantial fraction of the objects, about 45%, are in these two peaks.

We note in passing that there are no signs of lensing in the sample. We do not see multiple emission lines in the spectra, and

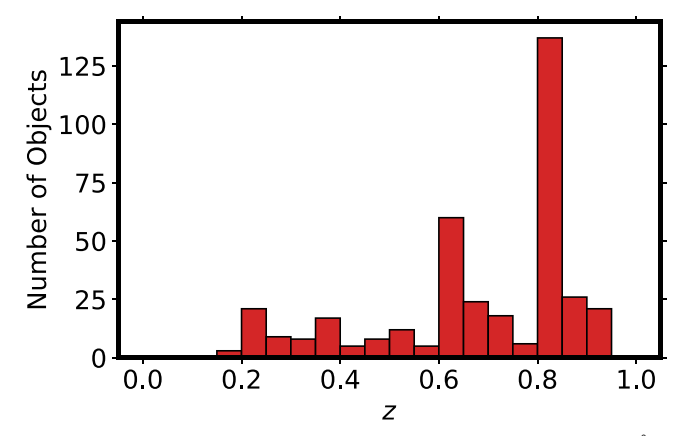


Figure 2. Redshift distribution for our high-EW sample (EW₀(H β) > 30 Å) of 380 galaxies. The bin width is 0.05 in redshift. The large excess present at z = 0.63 and z = 0.83 is due to overlap of H β and [O III] λ 5007 in the narrowband filters NB816 and NB921, respectively.

the objects are generally isolated. Since we are not concerned with luminosities and masses here, lensing would not affect our analysis.

3. Analysis

3.1. EW Measurements

To determine the metallicities of our sample, we measure the EWs of the emission lines of interest in each spectrum: [O II] λ 3727, [O III] λ 4363, [O III] λ 5007, and [N II] λ 6583, as well as H γ ,

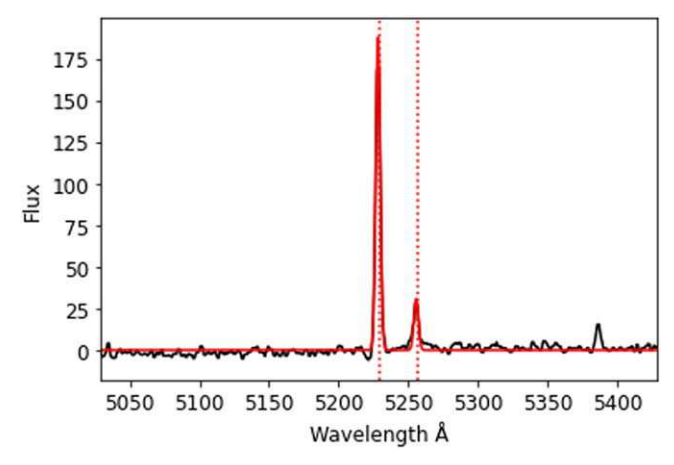


Figure 3. H γ and [O III] λ 4363 emission-line fit for the example galaxy in Figure 1. The red curve shows the fitted model that the EWs are determined from. The red dotted lines show the means of the fitted Gaussians.

 ${\rm H}\beta,$ and ${\rm H}\alpha.$ We use EWs instead of emission-line fluxes to avoid introducing biases from spectral flux calibrations. A challenge with determining EWs is measuring the continua of the spectra. We carefully inspected the spectra of all the sources with very weak continua to make sure that the continua are plausible. However, since we are primarily concerned with local line ratios, a continuum measurement is not critical to the metallicity determination. To measure the EWs, we simultaneously fit Gaussian functions to neighboring emission lines of interest, and we divide the integrated area under each fitted Gaussian by the median continuum level near each line. To convert these observed-frame EWs to rest-frame EWs, we divide by (1+z).

When fitting H β and the [O III] $\lambda\lambda4959$, 5007 doublet, we enforce a 3:1 internal ratio for the doublet and require that all three lines have the same line width. We fit a single redshift and assume that the FWHM is the same for all three lines. We fit the lines simultaneously using four free parameters (z, FWHM, and the amplitudes of the [O III] $\lambda5007$ and H β lines). We use the same procedure to fit simultaneously the H α line and the [N II] $\lambda\lambda6548$, 6583 doublet. We also use similar procedures to fit two Gaussian functions, with a single FWHM and redshift, to the H γ and [O III] $\lambda4363$ lines, as well as to the [O II] $\lambda\lambda3729$, 3727 doublet. We do not account for stellar absorption in the Balmer lines. Given the strength of the emission lines in EELGs, the effects of stellar absorption are extremely small.

By fitting multiple Gaussians simultaneously rather than individual lines independently, we increase the fidelity of the fits to weaker emission features. For example, [O III] $\lambda 4363$ is a relatively weak line compared to the neighboring H γ line. However, by simultaneously fitting H γ and [O III] $\lambda 4363$, we can infer the line center and line width from the stronger H γ line, thereby improving the fit to the weaker [O III] $\lambda 4363$ line. In Figure 3, we show the emission-line fit for the example galaxy shown in Figure 1.

Selecting EELGs increases the likelihood of getting [O III] λ 4363 detections. In Figure 4, we show all of the sources in our sample where H β is detected above a signal-to-noise ratio (S/N) of 20. For EW₀(H β) > 50 Å, 46 of the 70 sources are detected above a 2σ level in the [O III] λ 4363 line. For EW₀(H β) > 100 Å, only 4 of the 22 sources do not have >2 σ detections in [O III] λ 4363, and most sources have a very strong detection.

In Figure 5, we show a Baldwin, Phillips, and Terlevich (BPT) diagram (Baldwin et al. 1981) for the lower redshift sources in our sample that have $H\alpha$ measurements. We require

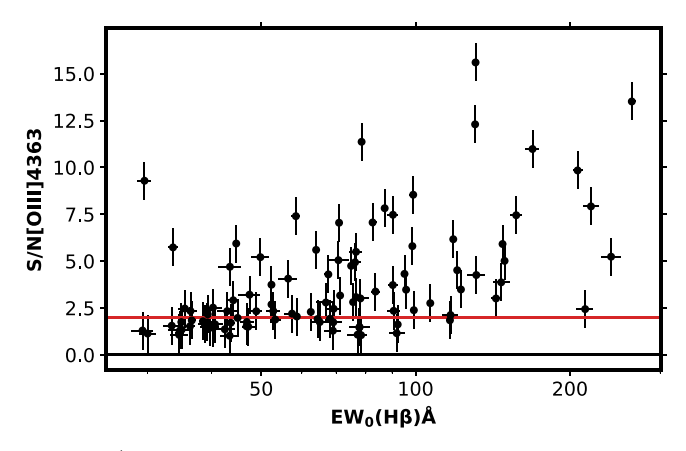


Figure 4. S/N of [O III] λ 4363 vs. EW₀(H β) for all the sources in our sample where H β is detected above an S/N of 20. The red line shows an S/N of 2 in [O III] λ 4363.

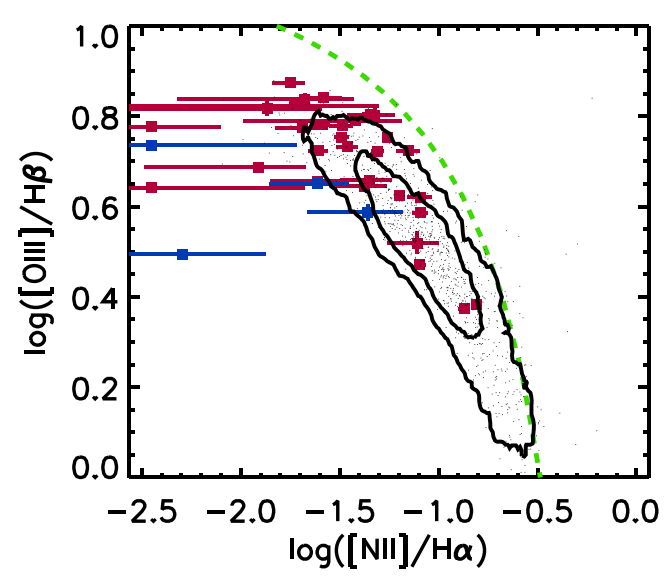


Figure 5. BPT diagram for all the sources in our sample where the $H\alpha$ line is on the spectrum and detected above an S/N of 20. The number density contours show the locus determined from the SDSS spectral sample. The dots show a subset of the SDSS data points. The green dashed curve shows the Kauffmann et al. (2003) separation between SFGs and AGNs. The red and blue points represent galaxies in our sample with $12 + \log (O/H) > 7.65$ and $12 + \log (O/H) \le 7.65$, respectively.

S/N > 20 in $H\alpha$ to choose sources where we can make a robust measurement of $[N II]/H\alpha$. We compare with the locus determined by the SDSS spectral sample. The figure demonstrates that our EW measurements are robust and that we have a spectral sample of SFGs that follow the BPT track. Although Figure 5 is limited to lower redshift sources due to the spectral coverage of [N II] and $H\alpha$, our higher redshift sources also do not show active galactic nucleus (AGN) signatures, such as $[NeV]\lambda 3426$. This suggests relatively little AGN contamination in the higher redshift part of the sample.

3.2. Flux Determinations

To convert the [O III] $\lambda 5007$ to [O III] $\lambda 4363$ EW ratio to a flux ratio, we use the relation

$$\frac{f(\lambda 5007)}{f(\lambda 4363)} = \frac{\text{EW}(\lambda 5007)}{\text{EW}(\text{H}\beta)} \times \frac{\text{EW}(\text{H}\gamma)}{\text{EW}(\lambda 4363)} \times \frac{f(H\beta)}{f(H\gamma)}.$$
 (1)

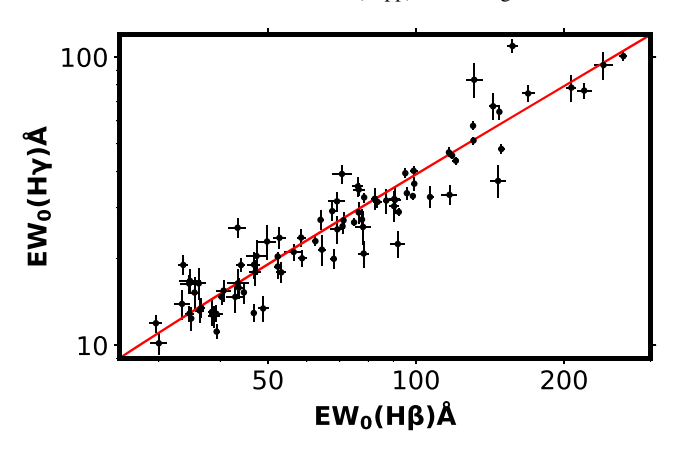


Figure 6. EW₀(H γ) vs. EW₀(H β) for all the sources in our sample where H β is detected above an S/N of 20. The Balmer decrement is shown by the red line, assuming the underlying continuum is flat in f_{ν} .

We assume the extinction in the sources is low and fix the flux ratio of $H\gamma$ to $H\beta$ at the Balmer decrement value of 0.47 (e.g., Osterbrock 1989). We also assume the continuum is flat between adjacent lines.

We may also compute flux ratios by assuming a shape for the underlying continuum. In Figure 6, we plot $\mathrm{EW}_0(\mathrm{H}\gamma)$ versus $\mathrm{EW}_0(\mathrm{H}\beta)$ for sources with $\mathrm{H}\beta$ S/N > 20. There is a near linear relation. Assuming the underlying continuum is flat in f_ν gives a median flux ratio for $\mathrm{H}\gamma$ to $\mathrm{H}\beta$ of 0.465, consistent with the Balmer decrement, which is shown by the red line. We use this method to compute the flux ratio of the combined [O II] $\lambda\lambda 3729$, 3727 doublet to the $\mathrm{H}\beta$ line. We consider this method more uncertain than the Balmer decrement method, which we use for the other line ratios.

3.3. Electron Temperature and Oxygen Abundance Determinations

In the T_e method, the metallicities of galaxies are deduced from the flux ratio of the $[O III]\lambda\lambda4959$, 5007 doublet to the $[O III]\lambda4363$ thermal line. We follow the prescription of Izotov et al. (2006) and use their Equations (1) and (2) to determine the electron temperatures.

Using the T_e method also allows ion abundances for galaxies to be derived directly from the strength of the emission lines, specifically O/H. Izotov et al. (2006) empirically fit relations to an electron temperature range for common galactic emission lines. This results in a large number of ionic abundance relations, including the desired O^+ and O^{2+} relations for this work (their Equations (3) and (5)). To obtain the total abundance of oxygen for each galaxy, these two equations must be added together. Note that there is typically little change in the total metallicity when adding O^+ to O^{2+} , as O^{2+} is the strongly dominant ionization state of oxygen in these galaxies. This means any uncertainties in our conversion of the EW ratio to flux ratio for $[O II]\lambda 3727/H\beta$ are less important.

3.4. Error Analysis

We first calculated the errors on the multi-Gaussian continuum fits. For each group of simultaneously fit emission lines, we shifted the positions of the fitted lines along the spectra in regular intervals, refitting the emission lines at each interval and calculating EWs. We then took the standard deviations of these EW measures as the 1σ error bounds on the

EWs of the lines. We used this method in order to properly sample the systemic, nonuniform noise in the spectra resulting from sky subtraction procedures.

To propagate the measurement errors we used a Monte Carlo technique, as analytical propagation would be needlessly complex. In this technique, we evaluated the oxygen abundance 10,000 times, using values drawn randomly from normal distributions for the EWs of $[O\ III]\lambda\lambda\lambda\ 5007,4959,4363$ H β , H γ , and $[O\ II]\lambda3727$, centered at the measured values, and with standard deviations corresponding to the 1σ errors on each value. We used the standard deviation of the distribution of total abundance for each galaxy as the 1σ error on the abundance of that galaxy. A general overview of the above error propagation procedure can be found in Andrae (2010).

4. Discussion

Following the procedures in Section 3, we determined the $12 + \log O/H$ abundance for each galaxy in our sample with S/N > 20 in the $H\beta$ line and detected above a 1σ threshold in $[O III]\lambda4363$. In Table 1, we summarize the 10 XMPGs found in this way. The two lowest metallicities are $12 + \log O/H = 6.949 \pm 0.091$ and 7.208 ± 0.061 at $EW_0(H\beta)$ of 169 ± 5 and 264 ± 4.69 Å, respectively. In Figure 7, we show the triple Gaussian fits to $H\beta$, $[O III]\lambda4959$, and $[O III]\lambda5007$ and the double Gaussian fits to $H\gamma$ and $[O III]\lambda4363$ for these two galaxies. We show the spectra of the remaining XMPGs in Figure 10, along with z-band images of the four XMPGs in the SSA22 field using newly reduced Subaru Hyper Suprime-Cam imaging (B. Radzom et al. 2022, in preparation) in Figure 11.

The majority of our objects have been identified in previous work. However, our present spectroscopic observations are significantly improved over those observations and allow for the detection of the [O III] λ 4363 Å line. Thus, our metallicity measurements for most of the objects are new. Two of our objects had previous metallicity measurements determined by Kakazu et al. (2007). In one case ($2^h40^m35^s56$, $-1^\circ35'37''.1$), the present 5 hr exposure is comparable to the 4 hr exposure used in Kakazu et al. (2007). In the other case ($22^h19^m06^s.30$, $+0^\circ47'21''.6$), the present 7 hr exposure is considerably longer than the 1 hr exposure used in Kakazu et al. (2007), and the errors are correspondingly lower. We include in Table 1, if available, the original source identification and the original metallicity determination.

In Figure 8, we show $12 + \log O/H$ abundance versus $EW_0(H\beta)$. Those galaxies not detected above 1σ in $[O\ III]$ $\lambda4363$ are shown at a nominal (high) value of 10. In examining the figure, a relation can be seen between $12 + \log O/H$ and $EW_0(H\beta)$. Specifically, as $EW_0(H\beta)$ increases, the metallicity decreases with a median metallicity of 8.39 for sources with $EW_0 = 50 - 100$ Å and 8.07 for sources with $EW_0 < 100$ Å. For the $EW_0 \ge 100$ Å region, a Pearson's correlation test gives a linear correlation factor (r-value) of -0.51 and a probability value of 0.02 for an uncorrelated system to produce the same r-value.

A simple linear fit between the O abundances and log $EW_0(H\beta)$ gives the relation

$$12 + \log(O/H) = 12.810 \pm 0.101$$

- $2.233 \pm 0.061 \times \log EW_0(H\beta) \text{ Å}$ (2)

for galaxies with EW₀ \geqslant 100 Å (black curve). We determined the errors on the fit by performing a Monte Carlo simulation

Table 1 All 10 XMPGs Discovered from the Final Spectral Sample of 380 Galaxies

R.A.	Decl.	$z_{\rm spec}$	$\mathrm{EW}_0(\mathring{\mathrm{A}})$					$12 + \log(O/H)$	Field	Exp
(J2000.0)		•	$_{ m H\gamma}$	[O III]λ4363	$_{ m Heta}$	[O III]λ4959	[O III]λ5007			(hr)
(1)	(2)	(3)	(4)	(5)	(6)	(7)	(8)	(9)	(10)	(11)
22 17 46.38 ^a	+0 18 13.0	0.8183	74.743 ± 4.939	41.609 ± 3.789	169.075 ± 5.004	217.107 ± 10.03	651.32 ± 10.023	6.949 ± 0.092	SSA22	19
22 19 06.30 ^b	$+0\ 47\ 21.6$	0.8175	100.766 ± 3.98	40.377 ± 2.987	264.084 ± 4.676	328.585 ± 6.434	985.756 ± 7.554	7.208 ± 0.061	SSA22	7
12 37 31.51°	$+62\ 10\ 6.0$	0.1724	16.402 ± 1.933	8.704 ± 1.853	43.443 ± 2.155	78.84 ± 1.691	236.521 ± 1.618	7.326 ± 0.18	HDFN	1
02 41 31.81 ^a	-1 33 14.8	0.3930	67.517 ± 7.056	13.113 ± 4.359	143.494 ± 2.8	149.177 ± 2.6	447.532 ± 4.029	7.333 ± 0.263	XMM-LSS	17
22 17 45.40 ^a	+0~28~18.4	0.6175	20.41 ± 2.757	8.17 ± 2.545	47.439 ± 2.255	72.363 ± 4.052	217.09 ± 3.099	7.338 ± 0.256	SSA22	6
02 40 35.56 ^b	$-1\ 35\ 37.1$	0.8206	22.911 ± 3.094	12.276 ± 2.355	49.809 ± 2.001	102.334 ± 1.795	307.002 ± 1.967	7.445 ± 0.167	XMM-LSS	5
03 34 09.78 ^d	$-28\ 1\ 28.0$	0.8540	93.78 ± 10.37	38.336 ± 7.321	240.602 ± 10.555	393.776 ± 12.252	1181.328 ± 14.547	7.477 ± 0.157	CDFS	5
10 44 51.69	+59 4 22.5	0.2295	20.815 ± 2.178	5.28 ± 5.025	78.292 ± 1.951	116.64 ± 5.454	349.92 ± 2.273	7.554 ± 0.551	Lockman	1
22 17 27.33 ^a	$+0\ 11\ 50.5$	0.3954	12.849 ± 3.351	3.086 ± 1.567	44.97 ± 1.518	70.539 ± 2.211	211.618 ± 1.789	7.61 ± 0.455	SSA22	10
10 33 03.85	+57 58 13.6	0.3370	12.965 ± 3.511	2.403 ± 1.762	42.458 ± 1.812	54.751 ± 1.233	164.252 ± 1.314	7.647 ± 0.547	Lockman	2

Notes. Right ascension is given in hours, minutes, and seconds, and decl. is given in degrees, arcminutes, and arcseconds.

a Identified in Kakazu et al. (2007).

b Objects with direct T_e metallicity determinations in Kakazu et al. (2007). The respective metallicities are $12 + \log(O/H) = 7.43^{+0.18}_{-0.15}$ and $12 + \log(O/H) = 7.43^{+0.22}_{-0.17}$.

c Identified in Ashby et al. (2015).
d Identified in Wold et al. (2014).

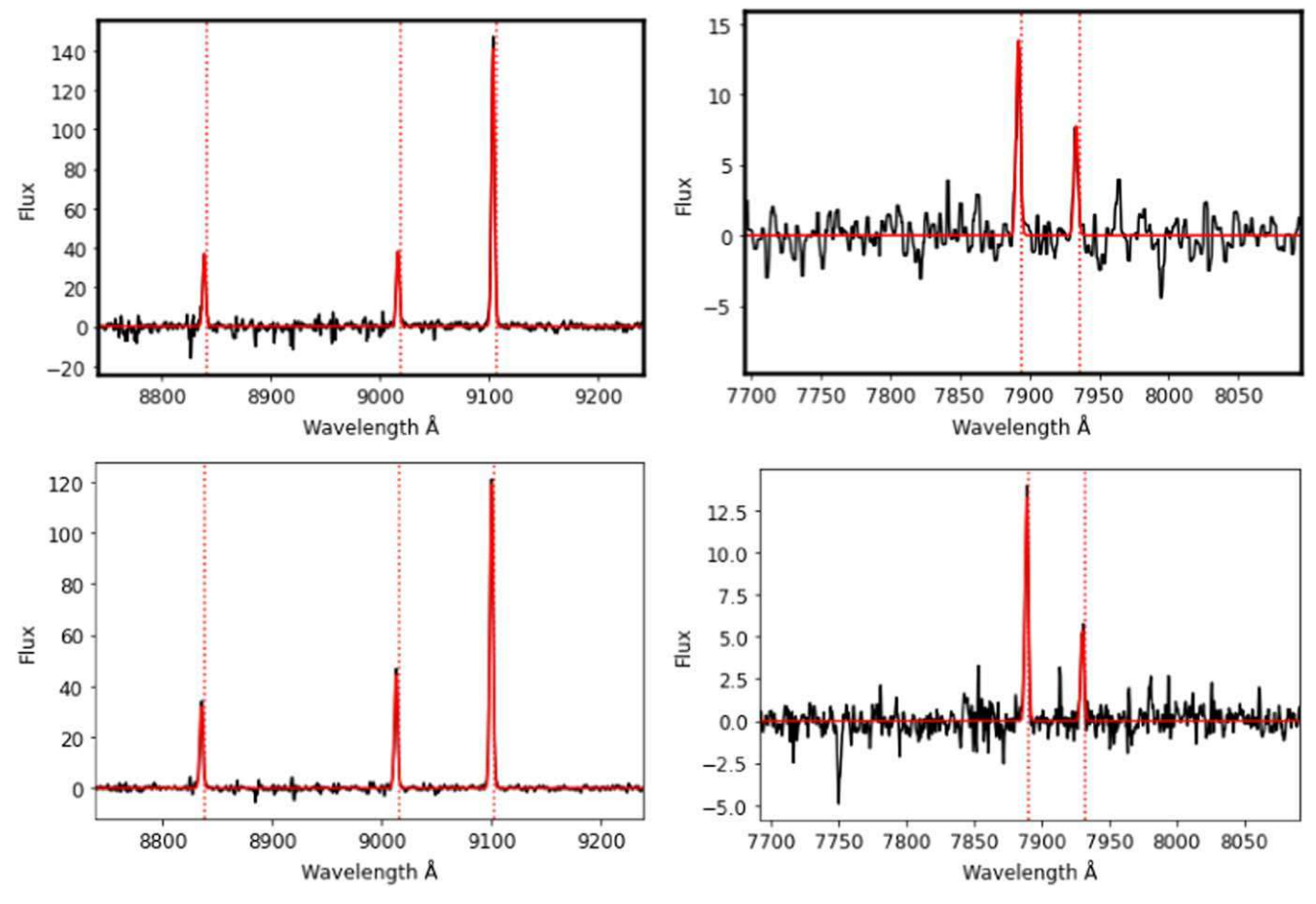


Figure 7. Left: emission lines $H\beta$, [O III] λ 4959, and [O III] λ 5007 in the (top) lowest-metallicity galaxy with $12 + \log O/H = 6.949 \pm 0.091$ and (bottom) second lowest-metallicity galaxy with $12 + \log O/H = 7.208 \pm 0.061$, along with their triple Gaussian fits. Right: emission lines $H\gamma$ and [O III] λ 4363 for the same two galaxies, along with their double Gaussian fits. A 5-point median smoothing has been applied.

based on the uncertainties in the $EW_0(H\beta)$ and metallicity of the data set. We show the 1σ distribution of the resulting set of fits in green shading in Figure 8. The minimum $EW_0(H\beta)$ requirement ensures the fitted relation accurately represents the higher $EW_0(H\beta)$ lower-metallicity region, which has been underconstrained in past XMPG surveys. This relation underlines the effectiveness of searching for XMPGs in samples of high-EW emission-line galaxies. To highlight the high-EW sample we focus on subsequently, we plot the data points at $EW_0(H\beta) < 100$ Å with fainter symbols, and we plot a vertical line at $EW_0(H\beta) = 100$ Å.

We are interested in the relationships between $EW_0(H\beta)$, metallicity, and galaxy age (t) at $EW_0(H\beta) \geqslant 100$ Å; specifically, the $EW_0(H\beta)$ evolution and the changes in metallicity as a function of galaxy age. By galaxy age, we mean the time since the onset of the currently dominant star formation episode. This does not preclude there being older underlying populations in the galaxy. To determine these relationships, we must first assume a star formation model.

We constructed instantaneous and continuous starburst models using the program Starburst99 (Leitherer et al. 1999; Vázquez & Leitherer 2005; Leitherer et al. 2010, 2014). We left the initial parameters for each Starburst99 model unchanged. We show the models in Figure 9.

In Figure 8, we see that the instantaneous starburst model, where the $EW(H\beta)$ drops very rapidly with time, is a poor fit to

our data at $\mathrm{EW_0(H\beta)} \geqslant 100\,\mathrm{\mathring{A}}$; thus, we focus our attention on the continuous starburst model. Specifically, we fit a power law to the continuous starburst model for $t > 10^7\,\mathrm{yr}$, which gives the relation

$$\log t(yr) = 12.956 - 2.700 \times \log EW(H\beta).$$
 (3)

In addition to our assumption that our galaxies are undergoing continuous starburst, we assume that (1) the oxygen abundance increases linearly with time, and (2) the hydrogen abundance remains constant throughout time. With these assumptions, we obtain the following relation between metallicity and age:

$$12 + \log O/H = \delta + \log t(yr), \tag{4}$$

or, combining with Equation (3),

$$12 + \log O/H = \delta + 12.956 - 2.700 \times \log EW_0(H\beta),$$
 (5)

where δ is a single fitted parameter, which is a measure of the yield.

We overplot Equation (5) on the distribution of galaxy metallicities for $\delta = 0.93$, which we chose to match the EW₀(H β) $\geqslant 100\,$ Å points (red curve). The blue curve is the instantaneous starburst model with the δ offset set to an arbitrary value. This curve is too flat to provide a fit to the data at EW₀(H β) $\geqslant 100\,$ Å.

The continuous starburst model shows reasonable agreement with the EW₀(H β) \geq 100Å data, but it overpredicts the EW₀(H β) < 100 Å data, suggesting that the effective yield or the

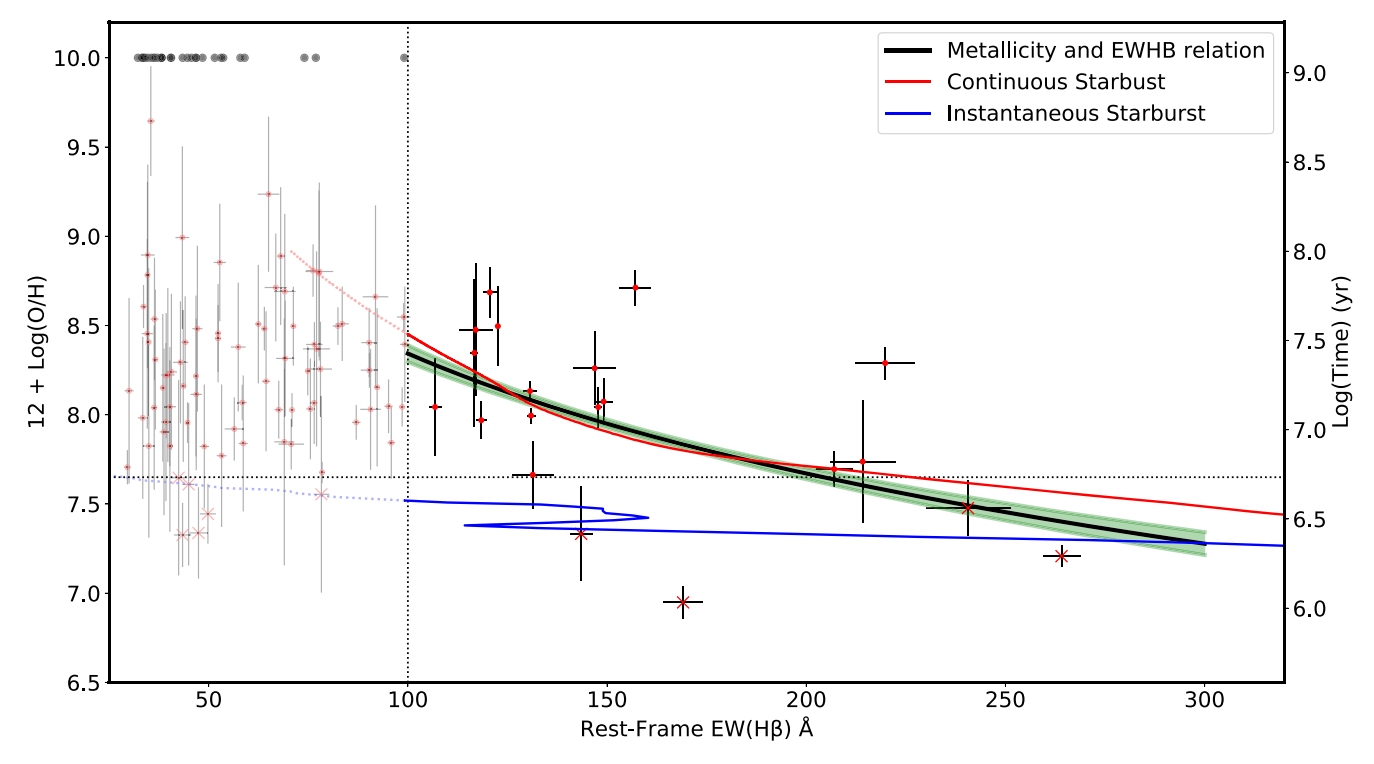


Figure 8. $EW_0(H\beta)$ vs. metallicity for our sample with S/N cuts of $H\beta \ge 20$ and $[O\ III]\ \lambda 4363 \ge 1$. Data that met the S/N cut of $H\beta \ge 20$ but not $[O\ III]\ \lambda 4363 \ge 1$ are plotted at a nominal value of 10. Prior $EW_0(H\beta)$ vs. metallicity plots suffered from a lack of galaxies populating the region where $EW_0(H\beta)$ exceeded 100 Å, and thus the overall shape of the relation was underconstrained. Here we see that as the rest-frame EW increases, the metallicity decreases. The black vertical dotted line shows the low metallicity threshold of $12 + \log (O/H) = 7.65$, which is 1/10 of the solar metallicity. The black solid curve represents a linear fit of $12 + \log(O/H) = 12.810 \pm 0.101 - 2.233 \pm 0.061 \times \log EW_0(H\beta)$ Å. We show the 1σ distribution of the Monte Carlo simulation fits in green shading. The metallicity abundance error and $EW_0(H\beta)$ error were determined from the procedures presented in Section 3.4. Also shown are the continuous (red curve) and instantaneous (blue curve) starburst models from Starburst99. We plot the data points at $EW_0(H\beta) < 100$ Å with fainter symbols and change each starburst model curve to dotted. We plot the XMPG sample as a different symbol to differentiate between our high-metallicity and low-metallicity sample. There is agreement between the metallicity and $EW_0(H\beta)$ relation and the continuous starburst model at high EWs, which underlines the dependence of metallicity and $EW_0(H\beta)$ on age.

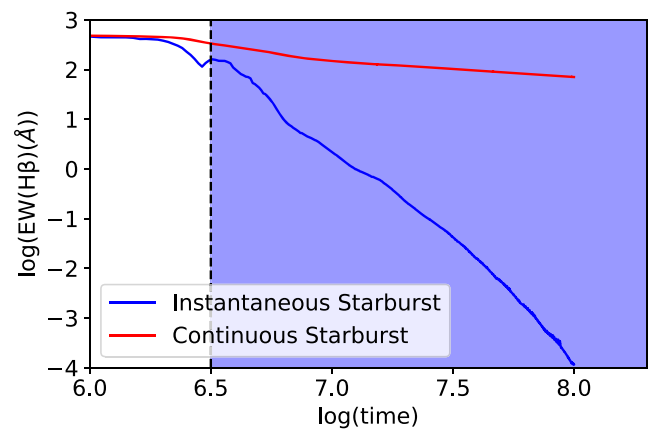


Figure 9. EW(H β) vs. time for the instantaneous (blue curve) and continuous (red curve) starburst models from Starburst99. The shaded region represents the time region of each model where we fit the models.

specific star formation rate is dropping with time. However, Figure 8 supports the main point, which is that there is a clear relation between EW₀(H β), age, and metallicity for EW₀(H β) \geqslant 100Å and that young XMPGs are undergoing star formation rates that are closer to continuous rather than instantaneous. Thus, for a galaxy with a measured EW₀(H β) \geqslant 100 Å, we can estimate the galaxy's age and the galaxy's metal abundance using Equations (3) and (5).

The models we test here do not exhaust the full range of possible parameter space of Starburst99, and thus do not

cover the full scope of star formation histories. Nonetheless, the continuous starburst model fits our high-EW sample well. The relation between $\mathrm{EW}_0(\mathrm{H}\beta)$ and metallicity is present due to the underlying relation of the two with the age of the galaxy.

In summary, we show that for $EW_0(H\beta) \ge 100 \text{ Å}$, $EW_0(H\beta)$ is a good proxy for galaxy age and metallicity, and XMPGs are best modeled by continuous starburst models.

5. Summary

In this study, we discovered eight new galaxies below the XMPG threshold of $12 + \log O/H = 7.65$ and improved upon metallicity measurements from Kakazu et al. (2007) for two more. Our lowest-metallicity galaxy has $12 + \log O/H = 6.949 \pm 0.091$. We compared metallicity and $EW_0(H\beta)$ for our spectral sample and found that at $EW_0(H\beta) \geqslant 100$ Å, there is a clear relation between the two, which we interpret as being a consequence of a near continuous star formation rate in the galaxy. For these sources, $EW_0(H\beta)$ is an adequate proxy for galaxy age and metallicity.

With the spectroscopic sample sizes continually increasing, we expect to find even lower-metallicity galaxies, which will help determine if there is a minimum galaxy metallicity in a given redshift range.

We thank the anonymous referee for very constructive comments that improved the manuscript. We gratefully acknowledge support for this research from the Diermeier Family Foundation Astronomy Fellowship (I.L.), NSF grant

AST-1715145 (A.J.B.), a Kellett Mid-Career Award and a WARF Named Professorship from the University of Wisconsin-Madison Office of the Vice Chancellor for Research and Graduate Education with funding from the Wisconsin Alumni Research Foundation (A.J.B.), the William F. Vilas Estate (A.J. T.), a Wisconsin Space Grant Consortium Graduate and Professional Research Fellowship (A.J.T.), and a Sigma Xi Grant in Aid of Research (A.J.T.).

The W. M. Keck Observatory is operated as a scientific partnership among the California Institute of Technology, the University of California, and NASA, and was made possible by the generous financial support of the W. M. Keck Foundation.

We wish to recognize and acknowledge the very significant cultural role and reverence that the summit of Maunakea has always had within the indigenous Hawaiian community. We are most fortunate to have the opportunity to conduct observations from this mountain.

Facilities: Keck:II (DEIMOS).

Software: Astropy Collaboration et al. (2013, 2018).

Appendix

Here we present the emission line fits for the remaining XMPGs in our sample as referenced in Section 4.

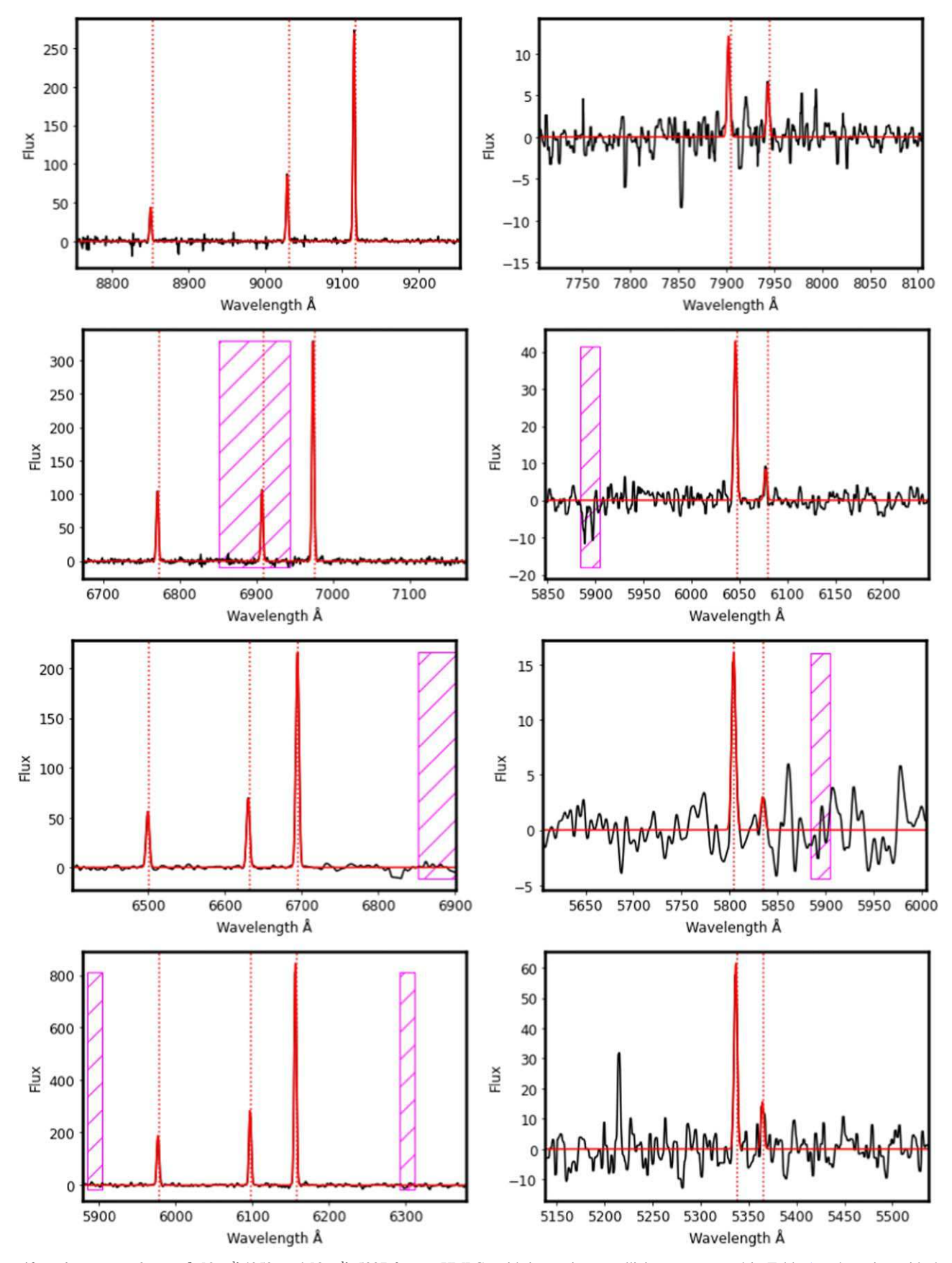


Figure 10. Left: emission lines $H\beta$, [OIII] λ 4959, and [OIII] λ 5007 for our XMPGs with increasing metallicity, as presented in Table 1 and starting with the third source, along with their triple Gaussian fits. Right:emission lines $H\gamma$ and [OIII] λ 4363 for the same galaxies, along with their double Gaussian fits. A 5-point median smoothing has been applied.

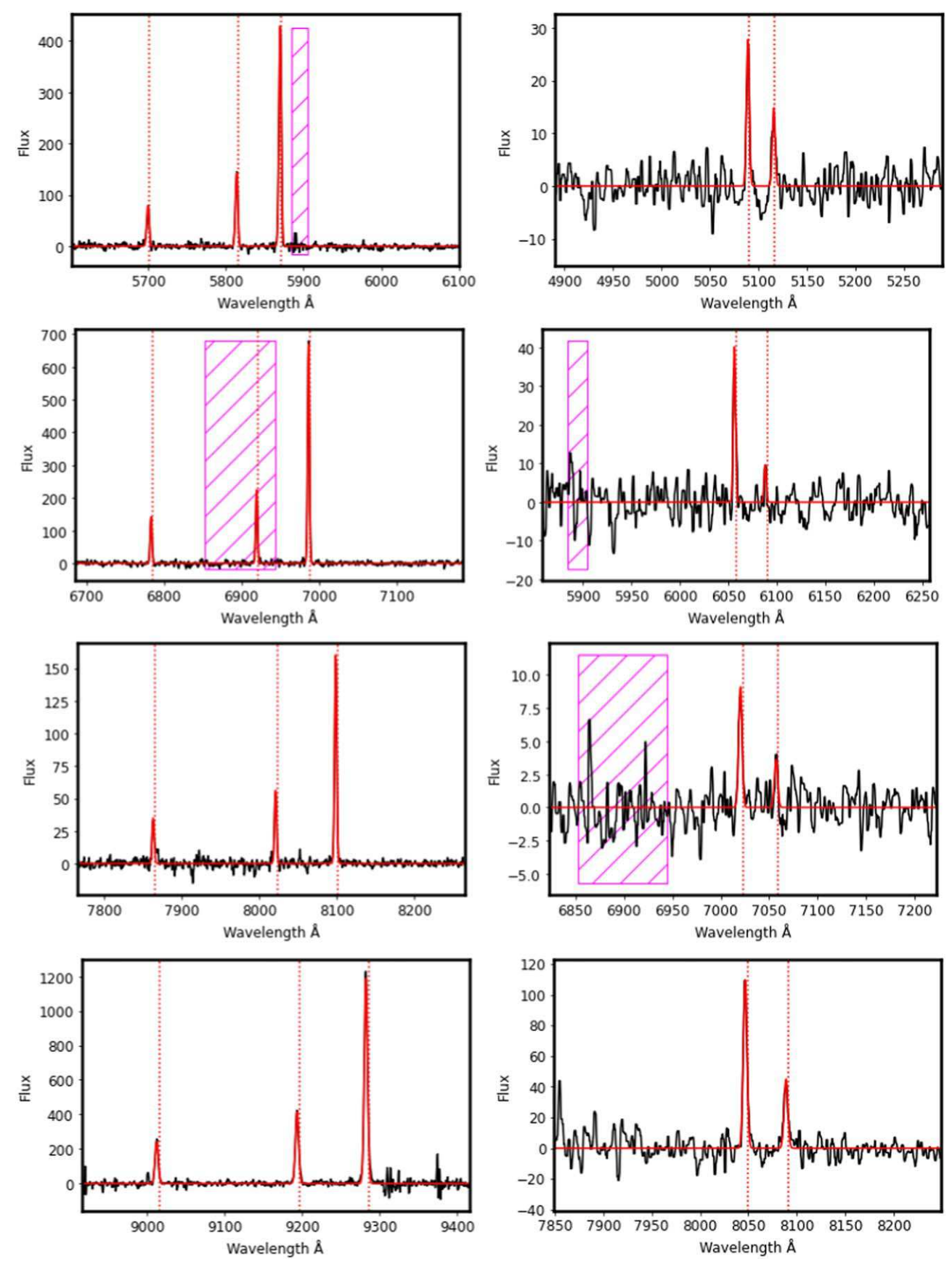


Figure 10. (Continued.)

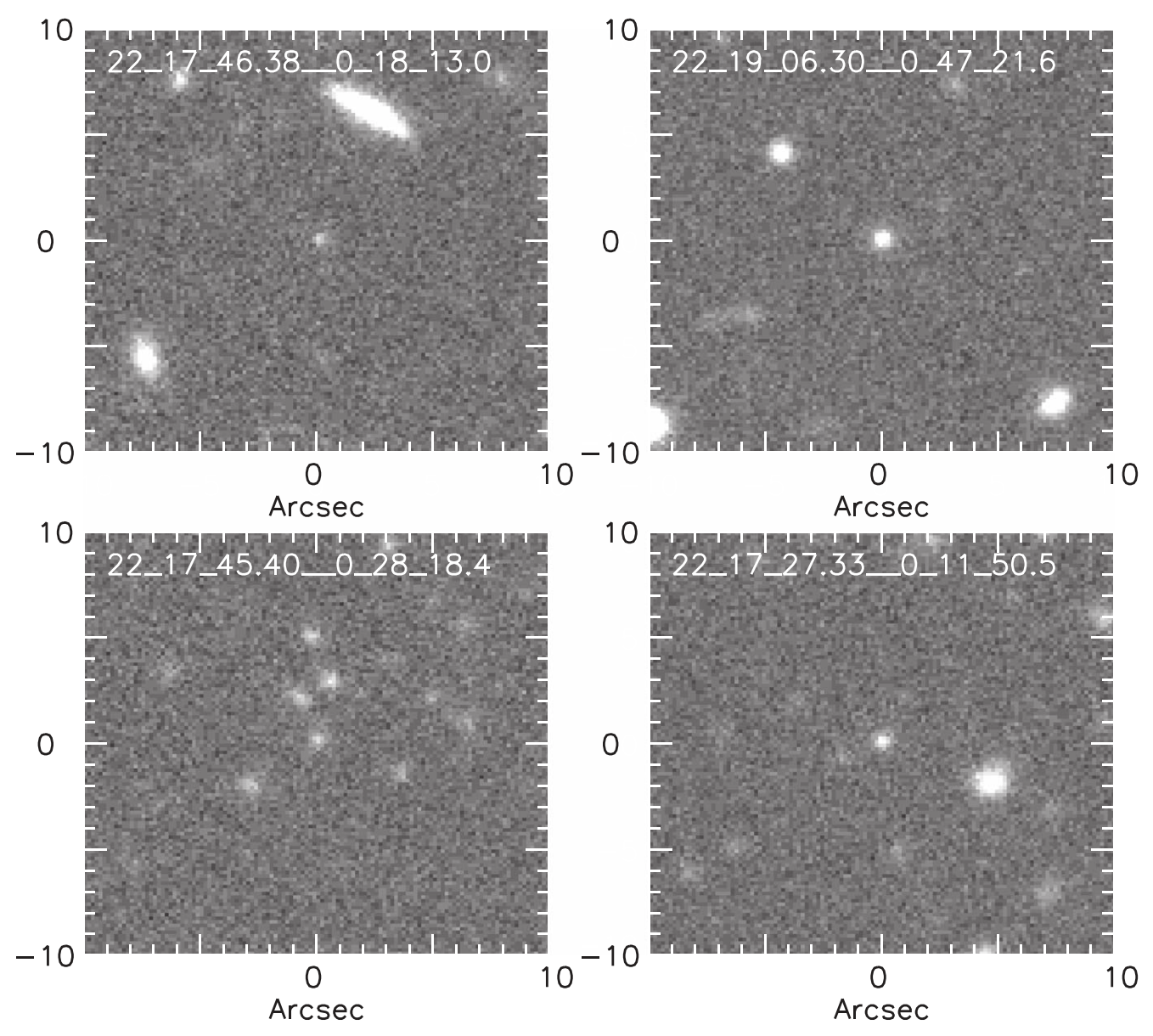


Figure 11. $20'' \times 20''$ newly reduced Subaru Hyper Suprime-Cam *z*-band imaging of our four XMPGs in the SSA22 field (B. Radzom et al. 2022, in preparation). As expected with high-quality imaging of XMPGs, we observe a sample of compact galaxies, which matches the morphology observed in other XMPG studies (e.g., Izotov et al. 2005, 2018; Hsyu et al. 2018; Kojima et al. 2020).

ORCID iDs

Isaac H. Laseter https://orcid.org/0000-0003-4323-0597 Amy J. Barger https://orcid.org/0000-0002-3306-1606 Lennox L. Cowie https://orcid.org/0000-0002-6319-1575 Anthony J. Taylor https://orcid.org/0000-0003-1282-7454

References

Amorín, R., Pérez-Montero, E., Contini, T., et al. 2015, A&A, 578, A105
Amorín, R., Sommariva, V., Castellano, M., et al. 2014, A&A, 568, L8
Andrae, R. 2010, arXiv:1009.2755
Ashby, M. L. N., Willner, S. P., Fazio, G. G., et al. 2015, ApJS, 218, 33
Asplund, M., Grevesse, N., & Jacques Sauval, A. 2006, NuPhA, 777, 1
Astropy Collaboration, Price-Whelan, A. M., Sipőcz, B. M., et al. 2018, AJ, 156, 123
Astropy Collaboration, Robitaille, T. P., Tollerud, E. J., et al. 2013, A&A, 558, A33
Baldwin, J. A., Phillips, M. M., & Terlevich, R. 1981, PASP, 93, 5
Barger, A. J., Cowie, L. L., & Wang, W. 2008, ApJ, 689, 687

Barger, A. J., Cowie, L. L., & Wold, I. G. B. 2012, ApJ, 749, 106 Cardamone, C., Schawinski, K., Sarzi, M., et al. 2009, MNRAS, 399, 1191 Cowie, Barger, & Songaila, A, A. J. 2016, ApJ, 817, 57 Cowie, L. L., & Barger, A. J. 2008, ApJ, 686, 72 Cowie, L. L., Barger, A. J., Hu, E. M., Capak, P., & Songaila, A. 2004, AJ, 127, 3137 Cowie, L. L., Songaila, A., Hu, E. M., & Cohen, J. G. 1996, AJ, 112, 839 Faber, S. M., Phillips, A. C., Kibrick, R. I., et al. 2003, Proc. SPIE, 4841, 1657 Hoyos, C., Koo, D. C., Phillips, A. C., Willmer, C. N. A., & Guhathakurta, P. 2005, ApJL, 635, L21 Hsyu, T., Cooke, R. J., Prochaska, J. X., & Bolte, M. 2018, ApJ, 863, 134 Hu, E. M., Cowie, L. L., Kakazu, Y., & Barger, A. J. 2009, ApJ, 698, 2014 Izotov, Y. I., Guseva, N. G., Fricke, K. J., et al. 2021, A&A, 646, A138 Izotov, Y. I., Stasińska, G., Meynet, G., Guseva, N. G., & Thuan, T. X. 2006, &A, 448, 955 Izotov, Y. I., Thuan, T. X., & Guseva, N. G. 2005, ApJ, 632, 210 Izotov, Y. I., Thuan, T. X., Guseva, N. G., & Liss, S. E. 2018, MNRAS, 473, 1956 Kakazu, Y., Cowie, L. L., & Hu, E. M. 2007, ApJ, 668, 853

```
Kauffmann, G., Heckman, T. M., Tremonti, C., et al. 2003, MNRAS, 346, 1055
Kojima, T., Ouchi, M., Rauch, M., et al. 2020, ApJ, 898, 142
Leitherer, C., Ekström, S., Meynet, G., et al. 2014, ApJS, 212, 14
Leitherer, C., Ortiz Otálvaro, P. A., Bresolin, F., et al. 2010, ApJS, 189, 309
Leitherer, C., Schaerer, D., Goldader, J. D., et al. 1999, ApJS, 123, 3
Liang, Y. C., Hammer, F., Yin, S. Y., et al. 2007, A&A, 473, 411
Ly, C., Malkan, M. A., Nagao, T., et al. 2014, ApJ, 780, 122
Nakajima, K., Ouchi, M., Xu, Y., et al. 2022, arXiv:2206.02824
Osterbrock, D. E. 1989, Astrophysics of Gaseous Nebulae and Active Galactic Nuclei (Mill Valley, CA: Univ. Science Books)
Pagel, B. E. J., Simonson, E. A., Terlevich, R. J., & Edmunds, M. G. 1992, MNRAS, 255, 325
```

```
Pilyugin, L. S., & Thuan, T. X. 2005, ApJ, 631, 231
Rosenwasser, B. E., Taylor, A. J., Barger, A. J., et al. 2022, ApJ, 928, 78
Salzer, J. J., Williams, A. L., & Gronwall, C. 2009, ApJL, 695, L67
Salzer, J. J., Feddersen, J. R., Derloshon, K., et al. 2020, AJ, 160, 242
Sargent, W. L. W., & Searle, L. 1970, ApJL, 162, L155
Senchyna, P, Stark, D, Chevallard, J, et al. 2019, MNRAS, 488, 3492
Seaton, M. J. 1975, MNRAS, 170, 475
Vázquez, G. A., & Leitherer, C. 2005, ApJ, 621, 695
Wold, I. G. B., Barger, A. J., & Cowie, L. L. 2014, ApJ, 783, 119
Wold, I. G. B., Finkelstein, S. L., Barger, A. J., Cowie, L. L., & Rosenwasser, B. 2017, ApJ, 848, 108
Yin, S. Y., Liang, Y. C., Hammer, F., et al. 2007, A&A, 462, 535
```